

A spectroscopic survey of Abell 1703: is it a rare relaxed cluster hosting a radio halo or a usual merging system?

W. Boschin,^{1,2,3*} M. Girardi,^{4,5} and F. Gastaldello⁶

¹Fundación G. Galilei - INAF (Telescopio Nazionale Galileo), Rambla J. A. Fernández Pérez 7, E-38712 Breña Baja (La Palma), Spain

²Instituto de Astrofísica de Canarias, C/Vía Láctea s/n, E-38205 La Laguna (Tenerife), Spain

³Departamento de Astrofísica, Univ. de La Laguna, Av. del Astrofísico Francisco Sánchez s/n, E-38205 La Laguna (Tenerife), Spain

⁴Dipartimento di Fisica dell'Università degli Studi di Trieste - Sezione di Astronomia, via Tiepolo 11, I-34143 Trieste, Italy

⁵INAF - Osservatorio Astronomico di Trieste, via Tiepolo 11, I-34143 Trieste, Italy

⁶INAF - IASF Milano, via E. Bassini 15, 20133, Milano, Italy

Accepted: 2019 December 23; Revised: 2019 November 27; Received: 2019 October 15

ABSTRACT

We present the study of the internal dynamics of the intriguing galaxy cluster Abell 1703, a system hosting a probable giant radio halo whose dynamical status is still controversial. Our analysis is based on unpublished spectroscopic data acquired at the Italian Telescopio Nazionale *Galileo* and data publicly available in the literature. We also use photometric data from the Sloan Digital Sky Survey. We select 147 cluster members and compute the cluster redshift $\langle z \rangle \sim 0.277$ and the global line-of-sight velocity dispersion $\sigma_v \sim 1300 \text{ km s}^{-1}$. We infer that Abell 1703 is a massive cluster: $M_{200} \sim 1 - 2 \times 10^{15} M_\odot$. The results of our study disagree with the picture of an unimodal, relaxed cluster as suggested by previous studies based on the gravitational lensing analysis and support the view of a perturbed dynamics proposed by recent works based on *Chandra* X-ray data. The first strong evidence of a dynamically disturbed cluster comes from the peculiarity of the BCG velocity with respect to the first moment of the velocity distribution of member galaxies. Moreover, several statistical tests employed to study the cluster galaxies kinematics find significant evidence of substructure, being Abell 1703 composed by at least two or three subclumps probably caught after the core-core passage. In this observational scenario, the suspected existence of a radio halo in the centre of this cluster is not surprising and well agrees with the theoretical models describing diffuse radio sources in clusters.

Key words: Galaxies: clusters: general. Galaxies: cluster: individual: Abell 1703. Galaxies: kinematics and dynamics.

1 INTRODUCTION

Radio haloes (also *giant radio haloes*, or GRHs) are diffuse sources found in the central regions of massive ($M_{200} \gtrsim 10^{15} M_\odot$) galaxy clusters. Extended over volumes of $\sim 1 \text{ Mpc}^3$, these low surface brightness features ($\sim 1 \mu\text{Jy arcsec}^{-2}$ at 1.4 GHz) have no obvious optical counterparts and roughly follow the intracluster medium (ICM) mass distribution. Their synchrotron steep-spectrum ($S(\nu) \sim \nu^{-\alpha}$; $\alpha > 1$) reveals the existence of a population of relativistic electrons and large-scale magnetic fields spread throughout the ICM (see, e.g., Feretti et al. 2012 for a review).

Until recently, GRHs were always discovered in merging clusters (e.g. van Weeren et al. 2019). Indeed, in the hierar-

chical scenario of cosmic structure formation, it is a common fact that galaxy groups and subclusters merge together into massive clusters. These processes release enormous amounts of gravitational energy (as large as 10^{64} erg; Sarazin 2002) and induce turbulence in the ICM, which is considered the key mechanism able to accelerate particles to relativistic energies (e.g. Brunetti & Jones 2015).

However, in the last years this picture got more complicated following the discovery of diffuse radio emission in several dynamically relaxed clusters. The first, impacting, case was the extended radio source found in the cluster CL1821+643 ($z \sim 0.296$; Bonafede et al. 2014, Boschin et al. 2018), whose size, location and power resemble that of typical GRHs despite the absence of any merging process responsible for its formation. Indeed, this case is not unique, since diffuse radio sources not powered by major mergers

* E-mail: boschin@tng.iac.es

have been recently discovered in more clusters in the redshift range 0.1–0.3. For instance, Abell 2390 and Abell 2261 (Sommer et al. 2017) are two more examples of cool-core clusters with Mpc-scale radio sources. Intriguing are also the cases of PSZ1G139.61+24 and Abell 2142. The first one hosts both a mini-halo (a feature typically found in cool-core relaxed systems, e.g. Gitti et al. 2018) and an underluminous and ultrasteepest spectrum radio halo (Savini et al. 2018a). Abell 2142, on its hand, is affected by minor merging activity, as suggested by the cold fronts detected in its ICM. However, as in the case of PSZ1G139.61+24, it also exhibits a double-component extended radio emission (Venturi et al. 2017), with a spectral steepness increasing in the outer regions. These two last examples could be hybrid sources, with mini-halos evolving into GRHs or viceversa (van Weeren et al. 2019). It is expected that the number of these “intermediate” cases will increase considerably in the near future thanks to observational facilities like LOFAR (van Haarlem et al. 2013).

Taking into account this new framework, in this paper we focus on Abell 1703 (hereafter A1703; Abell 1958, Abell et al. 1989), a system at $z \sim 0.28$ (Allen et al. 1992) whose dynamical status and radio properties might look like the ones of CL1821+643. In fact, several authors claim the possible existence of a radio halo in this cluster. The first hint comes from Owen et al. (1999; see their Table 2), who include A1703 in a list of nine clusters with diffuse radio emission. Indeed, A1703 is the brightest source in Owen et al. sample. More recently, the analysis of archival VLA data at 1.4 GHz showed some evidence of diffuse emission in the central region of the cluster (Govoni 2018, priv. comm.; see also our Fig. 1) despite contamination by radio pointlike sources (see Rizza et al. 2003 and our Sect. 2.1). Finally, Wilber (2018) highlights the presence in A1703 of possible radio halo emission at lower frequencies (120–168 MHz) in the LOFAR Two-Metre Sky Survey (LoTSS). This evidence is also confirmed by Savini et al. (2018b) in their Figure 8, where the contour levels at 144 MHz from LOFAR suggest the existence of a diffuse source in the location of the cluster.

On the other hand, the picture of A1703 that emerges at other wavelengths is controversial and suggest conflicting interpretations about the real dynamical status of this cluster. From the optical point of view A1703 is one of the richest clusters in the photometric catalogue of the SDSS (e.g. Koester et al. 2007) and presents a dominant giant elliptical cD galaxy in its centre (the brightest cluster galaxy; hereafter BCG). Moreover, this cluster shows impressive strong gravitational lensing features (Hennawi et al. 2008) which allowed to reconstruct its internal mass profile. For instance, Limousin et al. (2008), based on imaging data both from space (HST) and ground (Subaru), identified 13 systems forming highly-magnified images. Thanks to spectroscopic (from Keck) and photometric redshifts of these images they found that all the lensing systems can be reproduced by a single NFW (Navarro et al. 1997) profile for the dark matter, thus suggesting that A1703 is a regular, unimodal cluster. A follow-up study by Richard et al. (2009) based on further Keck spectroscopic measurements for seven multiple sources reinforced the evidence that A1703 is a relaxed cluster. More studies based on strong and/or weak gravitational lensing analysis also provided estimates of the cluster mass and the NFW concentration parameter. Even though the results are

quite discordant, they all coincide that A1703 is a massive system: $M_{\text{vir}} \simeq 1.1 - 2 \times 10^{15} M_{\odot}$ and $c_{\text{vir}} \simeq 3.3 - 7.1$ (Oguri et al. 2009, Zitrin et al. 2010, Oguri et al. 2012).

Such a large mass is also consistent with estimates derived from *Planck* observations of the thermal Sunyaev-Zeldovich effect. In fact, based on measurements of the Compton parameter Y and the $Y - M_{500}$ scaling relation of Arnaud et al. (2010), the Planck Collaboration (2016) reports an hydrostatic mass $M_{500}^{\text{SZ}} = 6.76_{-0.37}^{+0.35} \times 10^{14} M_{\odot}$, which corresponds to $M_{\text{vir}} \gtrsim 1 \times 10^{15} M_{\odot}$ assuming a NFW profile for the mass distribution.

As for the X-ray band, Piffaretti et al. (2011) report a measurement of the X-ray luminosity of A1703 from *ROSAT* data: $L_X(R < R_{500} = 1.07 \text{ Mpc}) = 5.42 \times 10^{44} \text{ erg s}^{-1}$ in the 0.1–2.4 keV band. Using eq. 10 of Böhringer et al. (2014), this luminosity translates to a mass estimate $M_{200} \gtrsim 1 \times 10^{15} M_{\odot}$ (in our cosmology, see below), again indicative of a massive cluster. Very recently, Ge et al. (2019) used unpublished *Chandra* archival data to compute the temperature of the ICM within 0.15–0.75 R_{500} : $kT_X = 9.63 \pm 0.75 \text{ keV}$. These data show that the ICM is elongated in the SSE–NNW direction (see contours in Fig. 1). However, despite the absence of obvious bimodality or more complex substructure, Ge et al. (2019) also report hints of a disturbed dynamics according to the measurements of several X-ray morphological parameters (see their Table 5) and their locations in the morphological planes of Cassano et al. (2010) and Mantz et al. (2015).

Taking into account the scenarios described by studies based on gravitational lensing and X-ray data, it is important to definitively establish whether A1703 is an anomalous relaxed cluster hosting diffuse radio emission or a common merging system. An exhaustive analysis of the kinematics of the cluster galaxy population could have the last word on the true dynamical status of this cluster. Moreover, this analysis would allow to study the possible presence of a merger along the line of sight, which would be difficult if not impossible to detect in the X-ray band. In fact, the spatial and kinematical study of member galaxies represent an effective tool to reveal substructures in clusters and put in evidence pre-merging subgroups or merger remnants (e.g. Boschin et al. 2004; Boschin et al. 2013).

With this context in mind, we used archival spectroscopic data obtained at the Italian Telescopio Nazionale *Galileo* (TNG) in order to perform the first dynamical analysis of this cluster based on member galaxies. These data sample the central ~ 1 Mpc size region of the cluster characterized by the diffuse X-ray and radio emissions. More data found in the NED Database, most of which obtained by Bayliss et al. (2014; hereafter B14) through spectroscopic measurements with MMT/Hectospec, allowed us to extend our spectroscopic sample to cover a wider area around the cluster (see Fig. 2).

This paper is organized as follows. Sect. 2 describes the TNG observations and data reduction and presents the velocity catalogue. In Sect. 3 we describe our member selection procedure. Sect. 4 and 5 explain the results of the analysis of the cluster structure. Finally, in Sect. 6, we discuss our results and present a portrait of the dynamical status of A1703.

Unless otherwise stated, we indicate errors at the 68% confidence level (hereafter c.l.). Throughout this paper, we use $H_0 = 70 \text{ km s}^{-1} \text{ Mpc}^{-1}$ in a flat cosmology with $\Omega_m = 0.3$

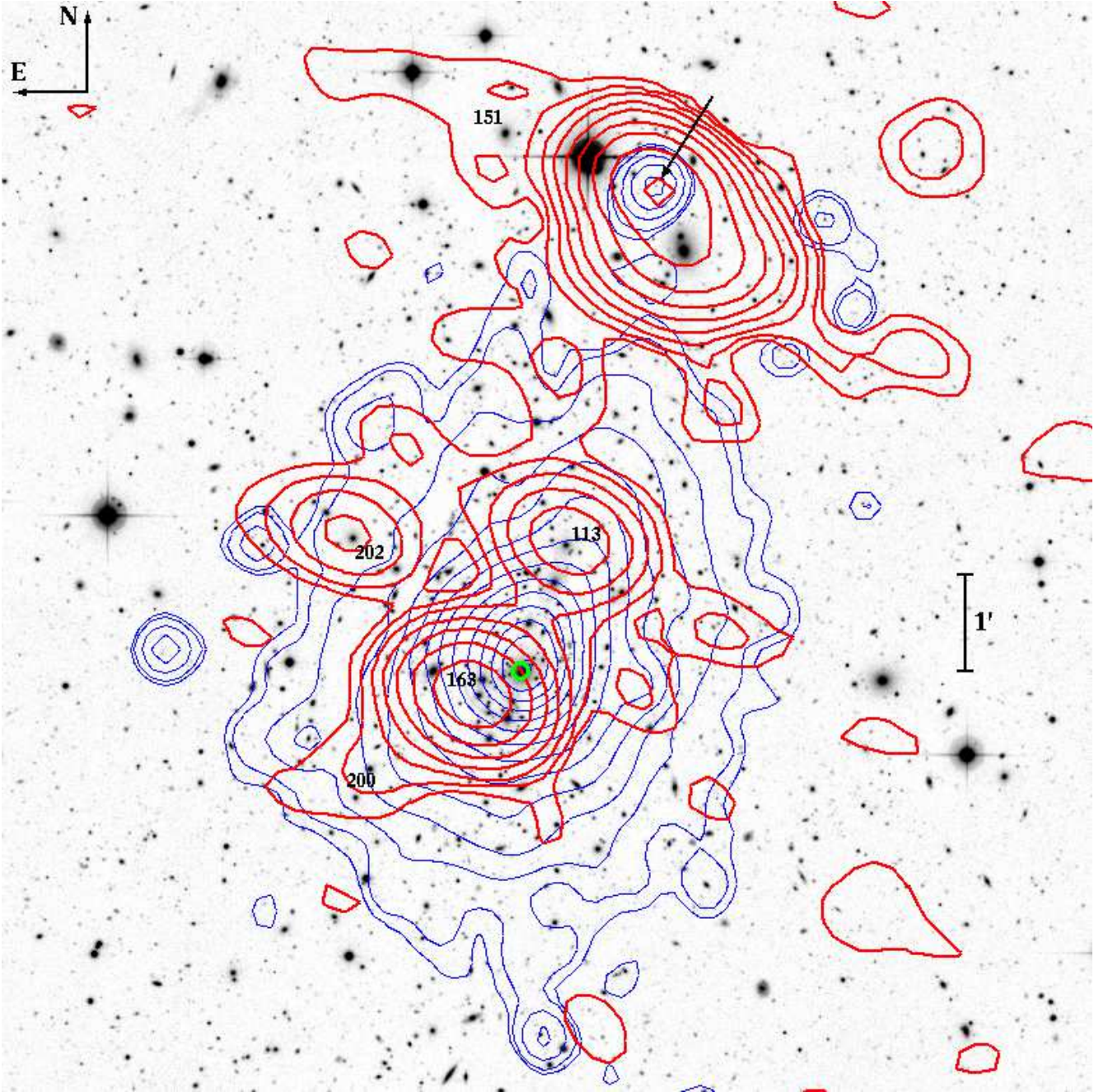


Figure 1. A multiwavelength picture of the cluster A1703. The gray-scale image in the background corresponds to the optical r -band (CFHT/Megaprime archival data). Blue thin contours show the cluster X-ray emission in the 0.5-2 keV band (from *Chandra* archival image ID 16126; Texp: 48 ks). Thick red contours are the contour levels of a VLA 1.4 GHz low-resolution image (courtesy F. Govoni; from archival VLA observation program AM 469). Numbers highlight member galaxies mentioned in the text. The green circle is the BCG (ID 141; see Table 1).

and $\Omega_{\Lambda} = 0.7$. In the adopted cosmology, $1'$ corresponds to ~ 253 kpc at the cluster redshift.

2 GALAXY DATA AND VELOCITY CATALOGUE

We used unpublished spectroscopic data stored in the TNG archive (<http://archives.ia2.inaf.it/tng>) taken in May 2010

(program A21TAC_50; PI: F. Gastaldello). These data consist of five MOS masks mainly sampling the central region of the cluster. Another mask was taken in June 2016 during a technical night. In particular, this last mask allowed to obtain the spectrum of the BCG. For all the six masks we used the LR-B Grism of the instrument DOLoRes¹ and

¹ <http://www.tng.iac.es/instruments/lrs>

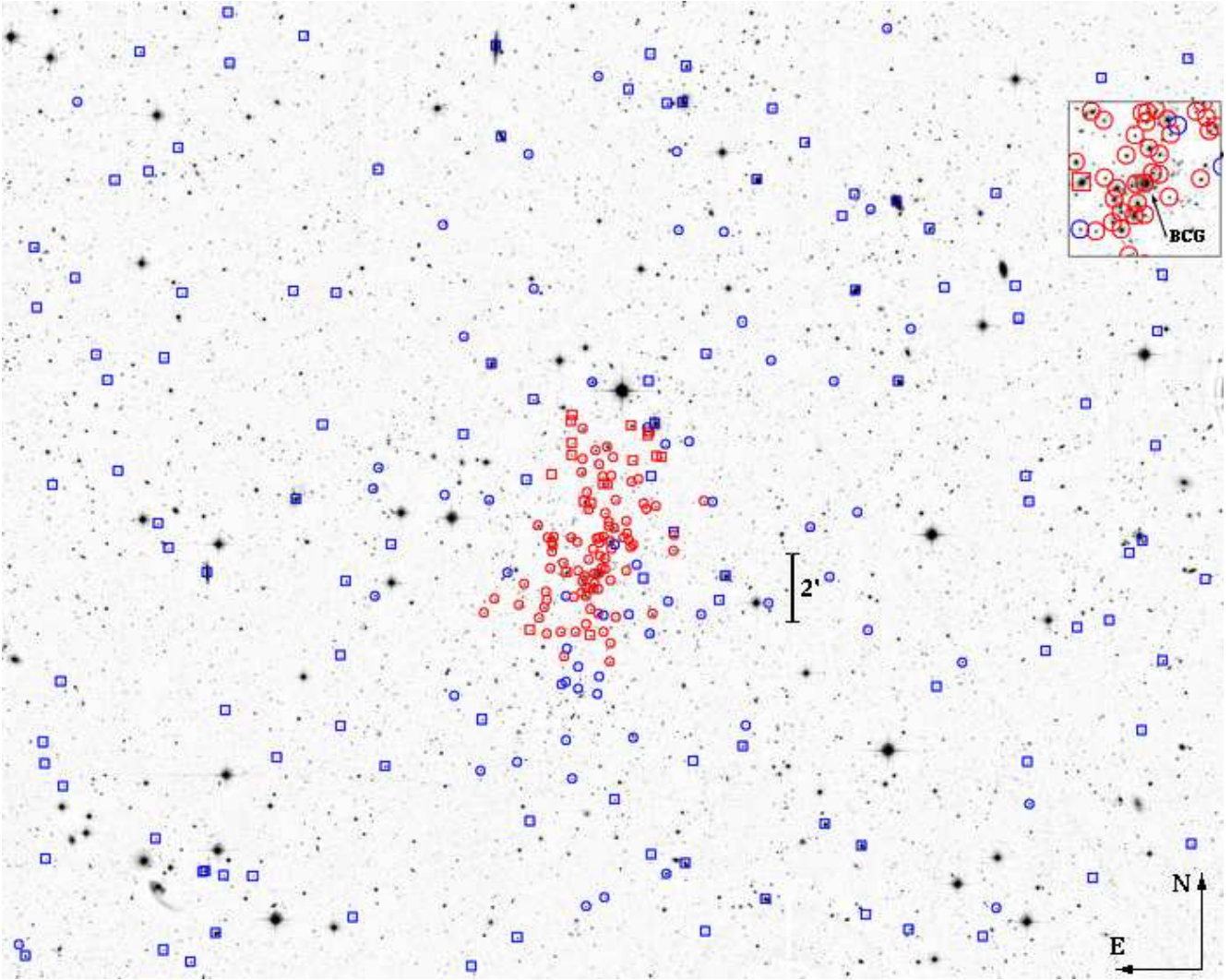


Figure 2. *r*-band wide field image (CFHT/Megaprime archival data) of the cluster A1703 showing the positions of all the galaxies of our spectroscopic catalogue. Circles and squares indicate cluster members and nonmember galaxies, respectively. Red symbols refer to galaxies observed at the TNG (see text and Table 1). Top right inset is a zoom on the central region of the cluster.

obtained spectra for 131 objects. The total exposure times varied from 3600s to 7200s.

We used standard IRAF tasks to reduce the spectra and adopted the cross-correlation technique (Tonry & Davis 1979) to compute redshifts for 104 targets. For 18 galaxies we obtained multiple redshift determinations. They allowed us to obtain a better estimate for the redshift errors. In particular, we found that the nominal cross-correlation errors are underestimated and multiplied them by a factor 2.5 (see Girardi et al. 2011 for details of the redshift computation and their errors). For another five galaxies (IDs. 117, 152, 154, 162 and 180; see Table 1), their redshifts were computed by measuring the wavelengths of the emission lines in their spectra.

In order to extend our spectroscopic sample to the outskirts of the cluster, we searched the NED database for galaxies with known redshift in the field of A1703. We found 184 objects within a radius of $\sim 20'$ from the cluster centre. Most of these objects (177) come from B14, ten of which are in common with our TNG data. To check for eventual

systematic deviations, we performed a straight-line fit to the TNG and B14 redshift measurements taking into account the errors on both data sets (see Chapter 15.3 of Press et al. 2007). We find an intercept $= (-2 \pm 8) \times 10^{-3}$ and a slope $= 1.01 \pm 0.03$ with a χ^2 probability $= 0.52$. Thus, we added the remaining 167 B14 galaxies and seven NED galaxies to our sample.

Our final spectroscopic catalogue includes 278 galaxies. The field of A1703 is covered by the SDSS. Its galaxy catalogue also provides us complete photometric information for all the galaxies of the spectroscopic sample in the magnitude bands *g*, *r*, and *i*.

Table 1 lists the velocity catalogue (see also Fig. 2): identification number of each galaxy, ID (Col. 1); redshift source (Col. 2; T:TNG, L:NED, B:B14); right ascension and declination, α and δ (J2000, Col. 3); (dereddened) SDSS *r* magnitude (Col. 4); heliocentric radial velocities, $V = cz_{\odot}$ (Col. 5) with errors, ΔV (Col. 6).

Table 1. Velocity catalogue of 278 spectroscopically measured galaxies in the field of A1703. IDs in italics refer to nonmember galaxies. Galaxy ID 141 (in boldface) is the BCG.

ID	Source	α, δ (J2000)	r	V (km s ⁻¹)	ΔV
<i>001</i>	B	13 13 13.66, +51 48 48.1	21.09	142509	69
<i>002</i>	B	13 13 16.19, +52 03 34.4	21.46	166775	96
<i>003</i>	B	13 13 16.50, +51 41 17.8	20.03	116430	27
<i>004</i>	B	13 13 21.13, +51 57 26.5	20.64	126545	36
<i>005</i>	B	13 13 21.59, +51 46 30.6	18.98	70250	30
<i>006</i>	B	13 13 22.20, +51 55 51.6	20.70	90154	54
<i>007</i>	B	13 13 22.63, +51 52 35.9	20.70	107578	75
<i>008</i>	B	13 13 25.19, +51 49 53.9	18.84	115294	18
<i>009</i>	B	13 13 25.56, +51 44 31.7	20.73	114710	39
<i>010</i>	B	13 13 27.59, +51 49 33.9	20.61	115480	111
<i>011</i>	B	13 13 31.36, +51 47 39.4	20.99	86817	66
<i>012</i>	B	13 13 32.20, +52 03 01.7	20.67	147285	39
<i>013</i>	B	13 13 34.59, +51 40 21.1	21.18	155562	54
<i>014</i>	B	13 13 35.50, +51 53 48.3	21.72	116685	33
<i>015</i>	B	13 13 37.34, +51 47 28.3	21.10	189304	57
<i>016</i>	B	13 13 43.03, +51 46 48.6	20.64	124402	54
<i>017</i>	B	13 13 45.96, +51 51 02.8	20.27	114620	63
<i>018</i>	B	13 13 46.21, +51 42 28.5	19.13	83693	33
<i>019</i>	B	13 13 46.53, +51 43 39.1	20.76	125199	33
<i>020</i>	B	13 13 46.65, +51 51 46.1	19.90	154438	27
<i>021</i>	B	13 13 47.76, +51 56 13.8	20.12	101459	51
<i>022</i>	B	13 13 48.24, +51 57 09.2	20.97	116841	84
<i>023</i>	B	13 13 51.79, +51 59 46.9	19.49	102676	33
<i>024</i>	B	13 13 52.32, +51 39 31.1	19.85	83369	39
<i>025</i>	B	13 13 54.87, +51 38 42.0	20.46	87818	45
<i>026</i>	B	13 13 58.50, +51 46 30.0	19.59	82845	30
<i>027</i>	B	13 14 01.35, +51 57 06.0	23.47	88999	84
<i>028</i>	B	13 14 03.13, +51 45 47.5	20.70	143175	69
<i>029</i>	B	13 14 04.11, +51 58 47.1	17.61	17850	150
<i>030</i>	B	13 14 07.66, +51 55 57.6	20.65	82893	60
<i>031</i>	B	13 14 08.32, +51 38 55.1	20.28	143490	42
<i>032</i>	B	13 14 09.91, +51 54 27.6	17.03	17982	150
<i>033</i>	B	13 14 10.21, +51 59 34.0	15.34	9875	150
<i>034</i>	B	13 14 11.77, +52 04 28.2	19.49	83207	36
<i>035</i>	B	13 14 14.92, +51 59 20.6	20.54	81654	48
<i>036</i>	B	13 14 15.76, +51 47 25.5	20.39	84610	42
<i>037</i>	B	13 14 16.22, +51 39 20.6	21.10	151044	45
<i>038</i>	B	13 14 16.99, +51 41 18.2	17.37	30336	150
<i>039</i>	B	13 14 17.60, +51 50 45.7	20.69	84365	42
<i>040</i>	B	13 14 17.76, +51 57 03.2	15.98	17586	150
<i>041</i>	B	13 14 17.93, +51 59 45.5	18.29	230894	150
<i>042</i>	B	13 14 20.11, +51 59 09.1	20.87	103548	63

2.1 Notable galaxies

A1703 is dominated by the galaxy ID 141 (the BCG). It is by far the brightest cluster member, being the magnitude difference with the second brightest member galaxy ~ 1.3 . Its colours ($g-r=1.58$ and $r-i=0.59$) well match the red sequences of cluster early-type galaxies (see our analysis of Sect. 5.2.1) and, consistently, its optical spectrum is that of an elliptical galaxy free of emission lines.

The field of A1703 is populated by several pointlike radio sources. Rizza et al. (2003; see their Table 3) report six sources from high spatial resolution ($\sim 1.5''$) VLA images at 20 cm. The counterparts of five of them are the member galaxies IDs. 113, 151, 163, 200 and 202 (see Fig. 1). The

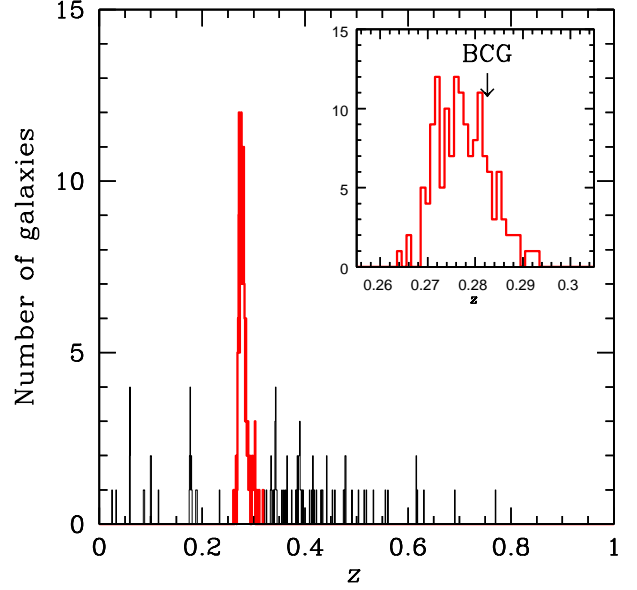


Figure 3. Redshift histogram of the galaxies of our spectroscopic sample. The solid red line histogram highlights the 170 galaxies assigned to A1703 by the 1D-DEDICA method. The distribution of the final 147 member galaxies with the indication of the BCG redshift is shown in the inset plot.

sixth one (n. 5 in Table 3 of Rizza et al. 2003), at $\sim 5.7'$ SW of the BCG, is not listed in our spectroscopic catalogue. Since its photometric redshift is 0.24 ± 0.04 (from the SDSS), it is unclear whether it is a cluster member or a foreground object. Finally, at $\sim 5'$ NNW of the BCG there is another strong radio source whose possible optical counterpart (highlighted by a black arrow on the top of Fig. 1) is also visible in the X-ray *Chandra* Image. Due to its faint magnitude ($r \sim 23$ from CFHT/Megaprime archival data) we argue that this object is a background AGN.

3 REMOVAL OF NONMEMBERS

The removal of nonmember galaxies was performed by using the two-step method called “P+G” (see, e.g. Biviano et al. 2013), which combines the 1D adaptive-kernel method DEDICA (1D-DEDICA; Pisani 1993) and the “shifting gapper” method (Fadda 1996). For the centre of A1703 we adopted the position of the BCG (RA=13^h15^m05^s.24, Dec.=+51°49′02.6″, see Table 1). The 1D-DEDICA method detected A1703 as a peak in the velocity space populated by 170 galaxies (see Fig. 3). Then, we rejected 23 galaxies from this provisional list of cluster members by using the “shifting gapper”, which combines the spatial and velocity information. The final sample contains 147 member galaxies (87 of which observed at the TNG), whose projected phase space is shown in Fig. 4.

4 GLOBAL PROPERTIES OF THE VELOCITY DISTRIBUTION

The biweight routines by Beers et al. (1990) provide robust estimates of the first moments of the velocity distribution.

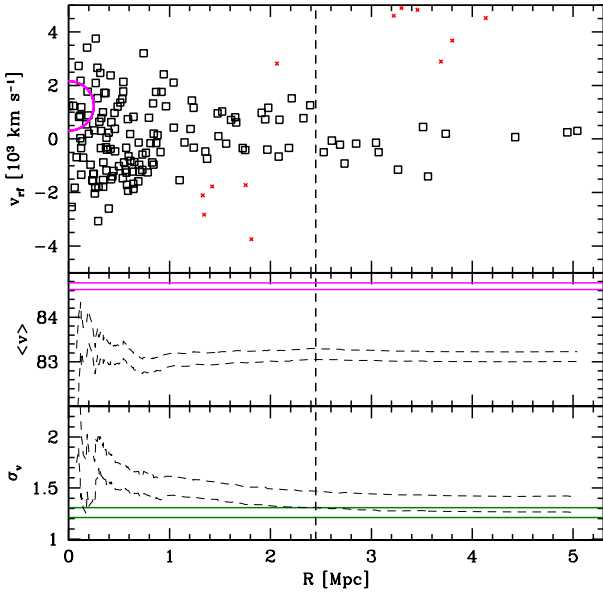


Figure 4. *Top panel:* Projected phase space diagram for the 147 member galaxies (squares) and nonmembers rejected with the shifting gapper procedure (small red crosses). Rest-frame LOS velocities are shown vs. projected clustercentric distance. The big magenta circle highlights the BCG. *Middle and Bottom panels:* Integral profiles of mean velocity and LOS velocity dispersion, respectively (only the one- σ error bands are shown). The mean (and dispersion) at a given (projected) radius R from the cluster centre is estimated by considering all galaxies within that radius (the first value computed on the five galaxies closest to the centre). For all the panels, the vertical black dashed line indicates R_{200} . In the central panel, the horizontal magenta lines show the one- σ error band of the BCG velocity. In the bottom panel, the horizontal green lines show the one- σ error band of the *Chandra* X-ray temperature (from Ge et al. 2019, see Sect. 1) converted to σ_v (see Sect. 6 for details).

Our measurement of the mean velocity is $\langle V \rangle = 83119 \pm 47$ km s $^{-1}$ (or $\langle z \rangle = 0.2773 \pm 0.0002$). The global line-of-sight (LOS) velocity dispersion is $\sigma_v = 1324^{+88}_{-71}$ km s $^{-1}$. Based on the σ_v - M_{200} relation of Munari et al. (2013), inferred from Λ -cold dark matter cosmological N -body and hydrodynamical simulations, we estimate a total cluster mass of $M_{200} = (2.2 \pm 0.6) \times 10^{15} M_{\odot}$ within $R_{200} = 2.45 \pm 0.15$ Mpc.

5 CLUSTER SUBSTRUCTURE

5.1 1D analysis of the velocity distribution

The 1D analysis refers to the study of the higher moments of the velocity distribution of member galaxies (Fig. 3). In particular, we find some evidence of deviation from Gaussianity according to the moments skewness and kurtosis (~ 90 – 95% and ~ 90 – 99% c.l., respectively). Moreover, there is also marginal evidence of asymmetry according to the asymmetry index (~ 90 – 95% c.l.; see Bird & Beers 1993 for details).

Very interestingly, the BCG has a significant ($> 99\%$ c.l.) peculiar velocity ΔV_{BCG} relative to the cluster mean velocity according to the Indicator test by Gebhardt & Beers

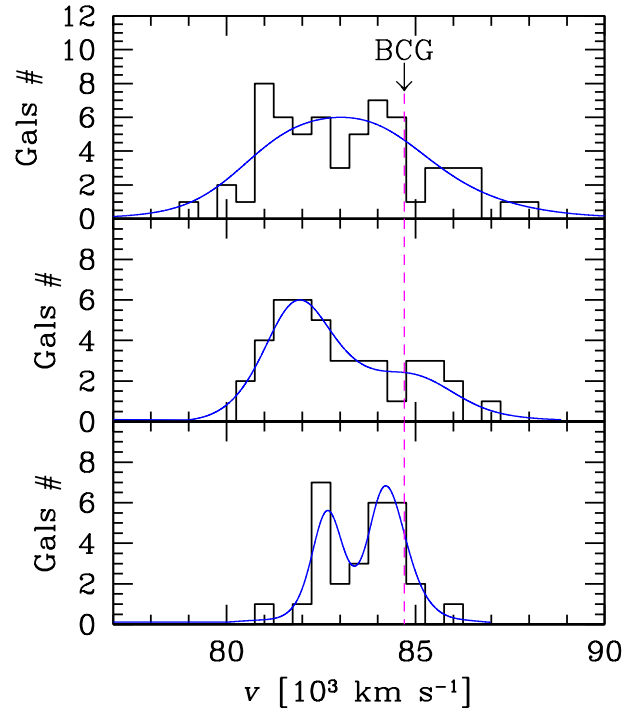


Figure 5. Velocity histogram of member galaxies in three projected clustercentric distance intervals: 0-0.5 Mpc (*top panel*), 0.5-1 Mpc (*middle panel*), and 1-2.5 Mpc (*bottom panel*). For all panels, blue curves show the number-galaxy density in the velocity space, as provided by the 1D-DEDICA method. The dashed magenta vertical line highlights the velocity of the BCG.

(1991). In particular, the absolute σ_v -normalized BCG peculiar velocity is $|\Delta V_{\text{BCG}}|/\sigma_v \sim 1.2$. This value puts the BCG of A1703 in the far tail of the $|\Delta V_{\text{BCG}}|/\sigma_v$ exponential distribution found by Lauer et al. (2014) studying a sample of 433 BCGs.

We then used the 1D-Kaye Mixture Model method (1D-KMM; Ashman et al. 1994). This test quantifies the statistical significance of bimodality (or more complex structure) in the velocity distribution with respect to a single Gaussian fit. The results are negative, i.e. there is no significant evidence of a two- or three-Gaussian partition. However, if we consider the velocity histograms obtained selecting member galaxies at different (projected) clustercentric distances (see Fig. 5) we unveil a more complex reality. In fact, while in the centre of the cluster ($R \leq 0.5$ Mpc) the velocity distribution is fitted by 1D-DEDICA with a single peak curve, at larger clustercentric distances signs of bimodality appear in the form of a fitted asymmetric curve. Then, for $R \gtrsim 1$ Mpc ($\sim 0.4 R_{200}$), the velocity distribution is clearly described by a two-peak curve. The significance of the two peaks, at ~ 82700 and ~ 84200 km s $^{-1}$, is $> 99.4\%$ c.l. according to 1D-DEDICA.

5.2 2D analysis of the galaxy distribution

About the analysis of the 2D spatial distribution of the spectroscopic member galaxies, we employed the 2D adaptive-kernel method of Pisani et al. (1996, hereafter 2D-DEDICA).

Table 2. Substructures detected by the analysis of the 2D distribution of the spectroscopic members of A1703. For each subclump, the 2D-DEDICA method provides the number of assigned member galaxies N_S , right ascension and declination of the density peak, the relative density with respect to the densest subclump ρ_S , and the χ^2 value of the galaxy peak.

Subclump	N_S	$\alpha(J2000), \delta(J2000)$ h : m : s, ° : ' : ''	ρ_S	χ^2_S
N	60	13 15 03.8, +51 49 50	1.00	33.9
S	59	13 15 06.1, +51 49 00	0.95	27.4

The results are shown in Fig. 6. The cluster is elongated along the SSE-NNW direction, in a similar way to the X-ray isophotes (see Fig. 1). Moreover, this test detects two dense galaxy peaks separated by only $\lesssim 1'$. The peak 'S' (see Table 2) is located close to the BCG (at $\sim 8''$ ESE), the peak 'N' is found at $\sim 9''$ SE of the galaxy ID 120. The eventual presence of luminosity segregation in a galaxy cluster can be a sign of disturbed dynamics (e.g. Maurogordato et al. 2011; see the discussion in Sect. 6). This motivates the exploration of the 2D galaxy distribution in different magnitude ranges. Very interestingly, running 2D-DEDICA only on the bright spectroscopic members ($r \leq 20$) the result is completely different with respect to the analysis of the whole spectroscopic sample: the two peaks and the elongation disappear. The distribution of bright members is now much more circular (see Fig. 7) with a centre close to the BCG and to the peak 'S'. Moreover, the distribution of faint spectroscopic members shows a peak in correspondence of the peak 'N'.

5.2.1 Analysis of the photometric sample

We are aware that the spectroscopic sample suffers from magnitude incompleteness. This is caused by constraints in the production process of the TNG MOS masks and the positioning of Hectospec fibers for the galaxies observed by B14.

The SDSS photometry of the cluster field is deep enough to help us alleviate our incompleteness problems. In particular, we select likely members on the basis of both ($r-i$ vs. r) and ($g-r$ vs. r) colour-magnitude relations (hereafter CMRs). The CMRs allow us to identify the cluster "red" early-type galaxies (i.e., the dominant cluster population, Dressler 1980) and to reduce the contamination by nonmember galaxies. We determine the CMRs by applying the 2σ -clipping fitting procedure to the cluster members and obtain $r-i=1.255-0.037 \times r$ and $g-r=2.365-0.045 \times r$ (see Fig. 8). Then, within the photometric catalogue we consider as likely "red" cluster members the galaxies with colour indexes $r-i$ and $g-r$ within 0.1 mag and 0.15 mag (i.e. the 1σ -error associated to the fitted intercept) of the respective CMRs.

Fig. 9 shows the contour map of the likely cluster members according to 2D-DEDICA. Again, we find that the distribution of bright galaxies ($r \leq 20$) shows just one peak and is only mildly elongated. Only if we consider fainter members (galaxies with $20 < r \leq 21.5$) we recover the SSE-NNW

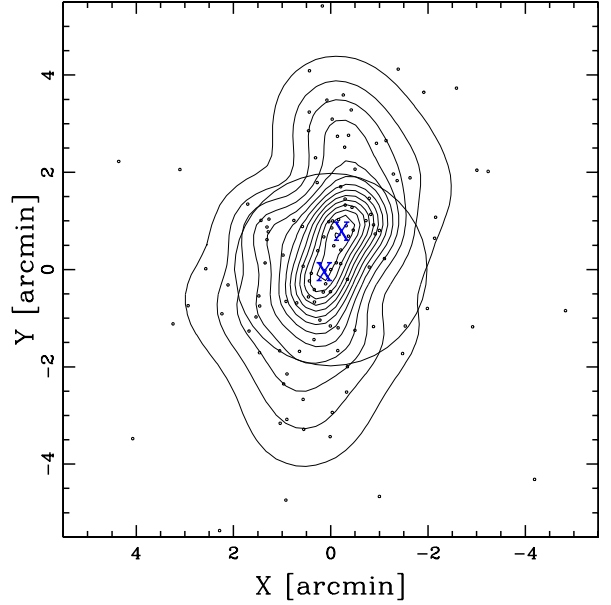


Figure 6. Spatial distribution of the spectroscopic cluster members in the central region of A1703 with, superimposed, the isodensity contour levels obtained with the 2D-DEDICA method. The blue crosses indicate the locations of the two galaxy peaks 'S' and 'N' (see also Table 2). The plot is centred on the cluster centre (the BCG) and circle contains the cluster within a radius equal to 0.5 Mpc.

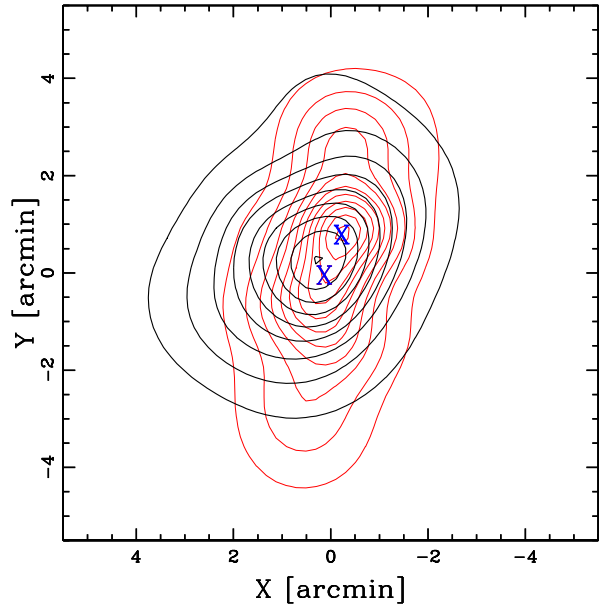


Figure 7. Isodensity contour map of the spectroscopic cluster members according to the 2D-DEDICA method. Black thick and red thin contours refer to bright ($r \leq 20$) and faint members, respectively (see text). The blue crosses indicate the locations of the galaxy peaks 'S' and 'N' (see Table 2). The plot is centred on the cluster centre (the BCG).

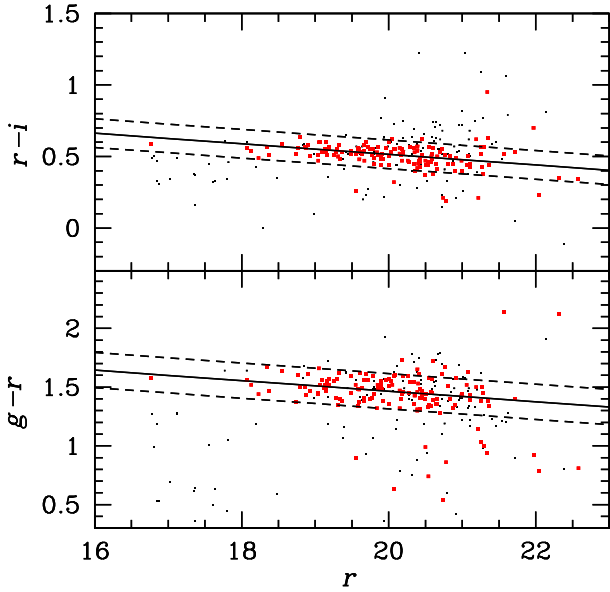


Figure 8. *Upper panel:* $r-i$ vs. r diagram for galaxies with available spectroscopic data. Red squares are cluster members, while black points represent field galaxies. The solid line shows the best-fit CMR as computed from cluster members; the dashed lines are drawn at $r-i \pm 0.1$ mag from the CMR (see text). *Lower panel:* $g-r$ vs. r diagram for galaxies with available spectroscopic data. As above, the solid line shows the best-fit CMR and the dashed lines are drawn at $g-r \pm 0.15$ mag from the CMR.

elongation with a maximum galaxy density close to the 'N' peak of Table 2.

This luminosity segregation is not a unique feature of A1703. In Sect. 6 we discuss this result in more detail.

5.3 3D analysis: combining velocity and position information

As for the 3D analysis, we employed different tools to search for a correlation between velocity and position information, which would be a clear sign of real substructures in the cluster.

First, we searched for an eventual velocity gradient by performing a multiple linear regression fit to the cluster velocity field (den Hartog & Katgert 1996). We find marginal evidence (at the $\sim 92\%$ c.l.) of a velocity gradient with $PA = 180 \pm 29$ degrees in the sample of the 147 spectroscopic cluster members. In particular, the southern region is populated by higher velocity galaxies.

Then, over the same sample we apply the classical Δ -test (Dressler & Schectman 1988, hereafter DS-test), which quantifies substructure searching for subsystems whose mean velocities and/or dispersions deviate from the global cluster values. Very significant substructure (at $> 99.9\%$ c.l., checked by running a Monte Carlo shuffling of the galaxy velocities; Dressler & Schectman 1988) is found in A1703 both with the “canonical” DS-test and its modified version, which consider only the local mean velocity as kinematical indicator (see also, e.g., Girardi et al. 2010 for more details). Again, high velocity galaxies tend to populate the southern region of the cluster.

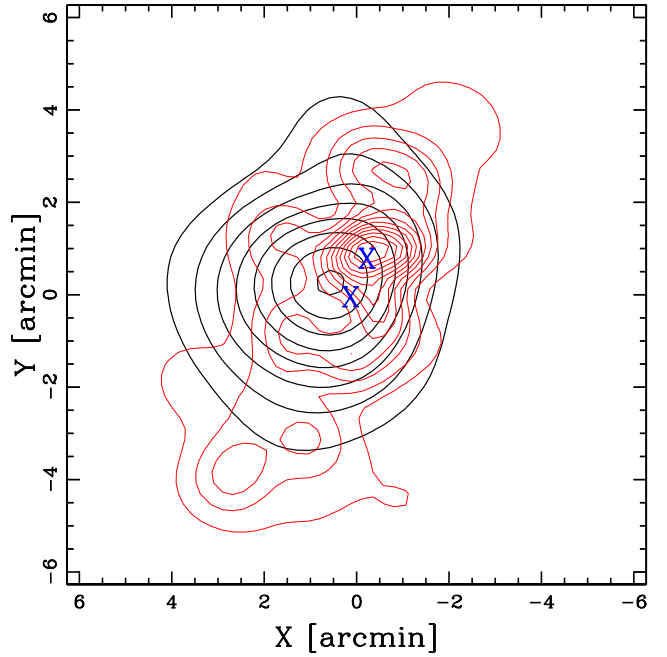


Figure 9. Isodensity contour map of the photometric likely cluster members according to the 2D-DEDICA method. Black thick and red thin contours refer to bright ($r \leq 20$) and faint members, respectively (see text). The blue crosses indicate the locations of the galaxy peaks 'S' and 'N' (see Table 2). The plot is centred on the cluster centre (the BCG).

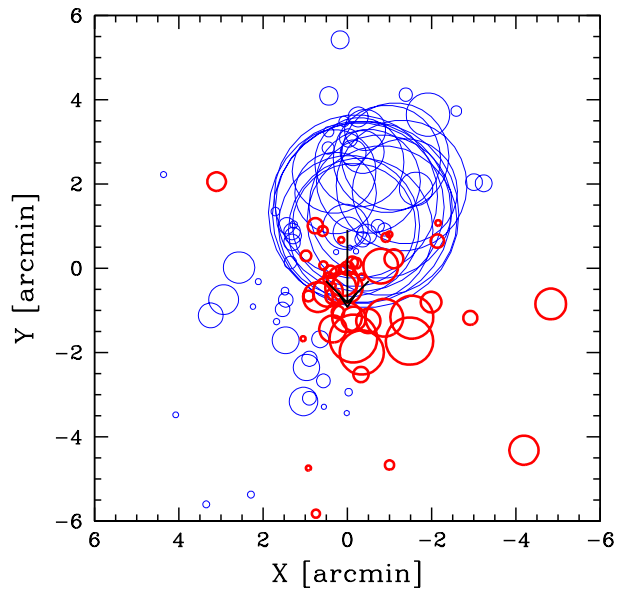


Figure 10. Spatial distribution of the cluster members in a $12' \times 12'$ box, each marked by a circle: the larger the circle, the larger is the deviation of the local mean velocity from the global mean velocity. In particular, thin/blue and thick/red circles show galaxies whose local value is smaller/larger than the global one according to the modified DS-test. The plot is centred on the cluster centre (the BCG). The black big arrow shows the direction of the velocity gradient (see text).

Table 3. Substructures detected by the 3D analysis of the spectroscopic members of A1703. For each subclump, the Htree method provides the number of assigned member galaxies N_S , the mean radial velocity with its error, and the radial velocity dispersion with its error.

Subclump	N_S	$\langle V \rangle$ km s ⁻¹	σ_v km s ⁻¹
G1	47	82022 ± 85	577 ± 48
G2	35	84681 ± 99	578 ± 75
G11	21	82466 ± 83	370 ± 69
G12	12	81242 ± 73	236 ± 72

Later, we resorted to the “hierarchical tree” (Htree) algorithm developed by Serna & Gerbal (1996; see also Adami et al. 2018 and Girardi et al. 2019 for recent applications). We apply it to the catalogue of 147 member galaxies. The method computes the relative binding energies of cluster galaxies and performs a hierarchical clustering analysis to detect galaxy subsystems.

The results of the Htree test are convincing: the cluster hosts two main substructures. In the centre of the dendrogram of Fig. 11 we find the group G2. It contains 35 galaxies and, in particular, the BCG. On the right the group G1 is the most prominent structure. It contains 47 galaxies and is itself substructured in two groups, G12 (12 galaxies) and G11 (21 galaxies). We run the Htree test by assuming a constant value of $M/L_r=150 M_\odot/L_{r,\odot}$ for the mass-to-light ratio of galaxies, but the results are quite robust against the adopted value of M/L_r .

In Table 3 we report the properties of the subclumps found with the Htree method.

In Fig. 12 we show the positions of the galaxies belonging to the groups G1 and G2. G1 galaxies have lower velocities and populate mainly the northern region of the cluster.

Note that the velocity dispersions of the groups of Table 3 are probably underestimated, since they do not include all the galaxies of the cluster and could just be the cores of more massive structures. To overcome this point we used the 3D version of the KMM test (3D-KMM). In particular, we used the galaxy assignments of the groups G1 and G2 as a first guess when fitting two groups. The algorithm fits a two groups partition at the 98.4% c.l. The results for the two groups are reported in Table 4. Based on the estimates of the velocity dispersions of the two groups, we find from Munari et al. (2013): $R_{200} = 1.45 \pm 0.1$ Mpc and $M_{200} = (4.6 \pm 1.6) \times 10^{14} M_\odot$ for KMM3D1, $R_{200} = 1.6 \pm 0.2$ Mpc and $M_{200} = (5.8 \pm 2.6) \times 10^{14} M_\odot$ for KMM3D2. Therefore, the total mass would be $M_{200} = (10.4 \pm 3) \times 10^{14} M_\odot$.

Finally, the substructure found by the Htree test is confirmed by the analysis performed with the three dimensional adaptive-kernel method of Pisani (1993, 1996; 3D-DEDICA). The results are reported in Table 5, where the three groups DED3D1, DED3D2 and DED3D3 correspond to the groups G2, G12, and G11 detected by the Htree method.

Table 4. Substructures detected by the 3D analysis of the spectroscopic members of A1703. For each subclump, the 3D-KMM method provides the number of assigned member galaxies N_S , the mean radial velocity with its error, and the radial velocity dispersion with its error.

Subclump	N_S	$\langle V \rangle$ km s ⁻¹	σ_v km s ⁻¹
KMM3D1	86	82119 ± 85	782 ± 66
KMM3D2	61	84608 ± 109	845 ± 97

Table 5. Substructures detected by the 3D analysis of the spectroscopic members of A1703. For each subclump, the 3D-DEDICA method provides the number of assigned member galaxies N_S , the fitted radial velocity V_{fit} , right ascension and declination of the density peak, the relative density with respect to the densest subclump ρ_S , and the χ^2 value of the galaxy peak.

Subclump	N_S	V_{fit} km s ⁻¹	$\alpha(\text{J2000}), \delta(\text{J2000})$ h : m : s, ° : ' : "	ρ_S	χ_S^2
DED3D1	49	84346	13 15 04.9, +51 49 12	0.40	30
DED3D2	43	81242	13 15 02.8, +51 50 16	1.00	44
DED3D3	26	82771	13 15 07.9, +51 48 36	0.32	20

6 DISCUSSION AND CONCLUSIONS

The value of the global velocity dispersion $\sigma_v = 1324_{-71}^{+88}$ km s⁻¹ (in agreement with the estimate of B14) is typical of a massive cluster and is consistent with the X-ray temperature $kT_X = 9.63 \pm 0.75$ keV measured by Ge et al. (2019) under the assumption of energy density equipartition between galaxies and ICM. In fact, we find $\beta_{\text{spec}} = \sigma_v^2 / (kT_X / \mu m_p) = 1.10_{-0.15}^{+0.17}$.

A value of $\beta_{\text{spec}} \sim 1$ is not anomalous for a dynamically relaxed cluster as A1703 was thought to be until very recently. However, we find convincing evidence that this cluster is experiencing a merger of two or more subclumps. The first hint of a disturbed dynamics comes from the 1D analysis of the galaxy velocity distribution. Even if its statistical moments suggest only marginal evidence of deviation from the Gaussianity, the velocity distributions of member galaxies at various clustercentric distances (see Sect. 5.1 and Fig. 5) point out the possible existence of two galaxy populations with different mean velocities (separated by ~ 2000 km s⁻¹) but well mixed in the central ($R \lesssim 1$ Mpc) region of the cluster. However, the most compelling argument in favour of an ongoing merger in A1703 comes from the very significant peculiar velocity of the BCG (e.g. Martel et al. 2014). This is in sharp contrast with what is usually found in regular clusters, where the dominant galaxy is well placed at the peak of the global velocity distribution (as in the case, e.g., of CL1821+643; Boschin et al. 2018).

About the 2D analysis of the galaxy distribution, the 2D-DEDICA method applied on the whole set of 147 member galaxies shows that the cluster is elongated in the SSE-NNW direction (Fig. 6) with two closely spaced peaks (see Table 2), another sign that at least two subclumps are in the process of merging. Indeed, if we consider only bright

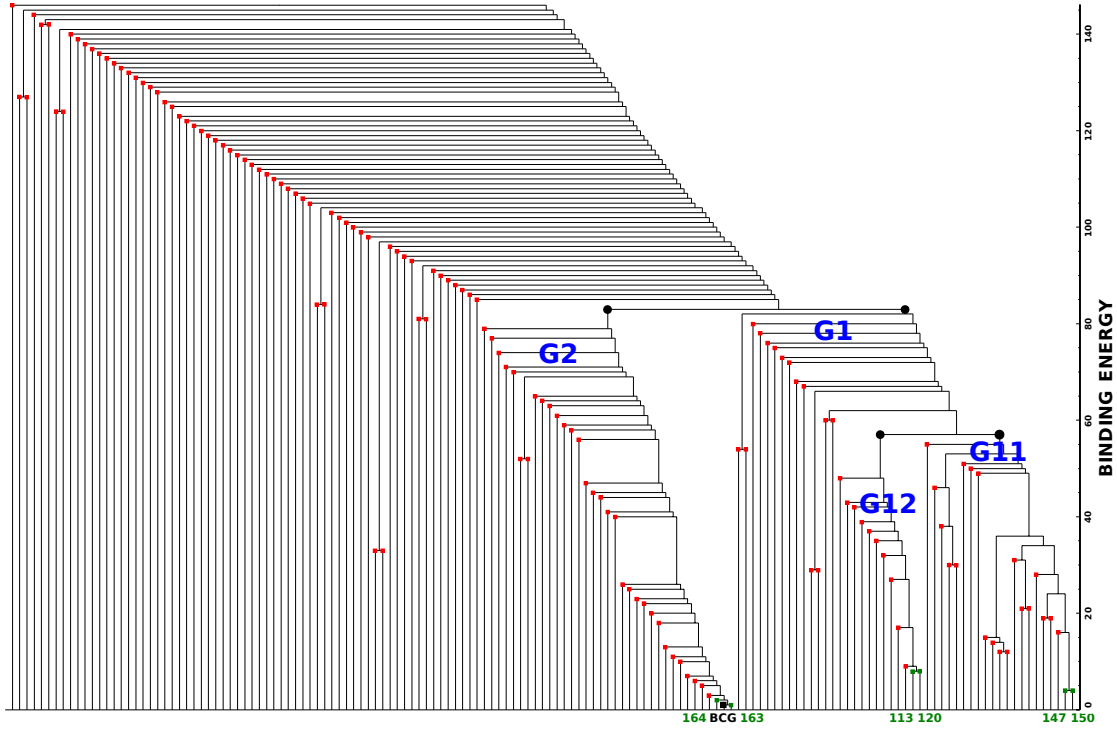


Figure 11. Dendrogram obtained through the Serna & Gerbal algorithm adopting $M/L_r=150 M_\odot/L_{r,\odot}$. The y-axis is the binding energy, here in arbitrary units with the lowest energy levels on the bottom. Labels indicate prominent galaxies and structures.

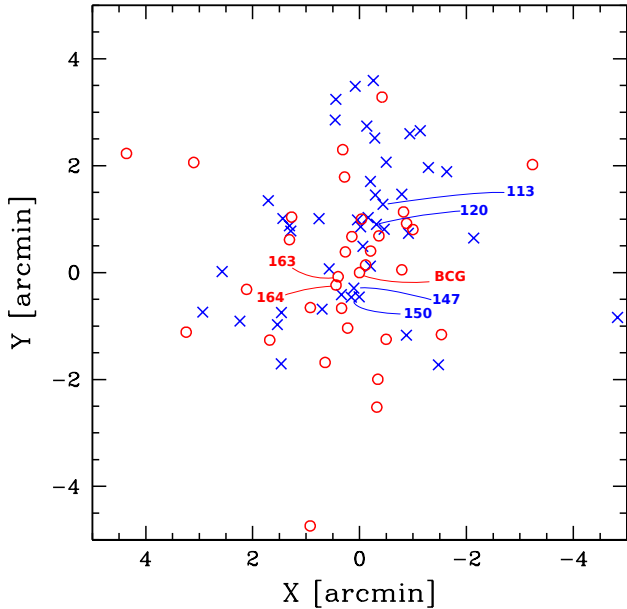


Figure 12. Member galaxies belonging to the groups G1 (blue crosses) and G2 (red circles) in a $10' \times 10'$ box centred on the BCG. Labels highlight galaxies at the lowest binding energy levels of their respective groups (see Fig. 11).

members with $r \leq 20$, their spatial distribution is much more circular and exhibits only one peak close to the BCG and the peak 'S'. We remark that this luminosity segregation is confirmed also by the 2D analysis of the photometric mem-

bers distribution, thus it does not seem an artifact of the incompleteness of the spectroscopic sample. Moreover, note that the peak 'N' and the density peak observed in the distribution of faint member galaxies (Figs. 7 and 9) coincide with a secondary mass peak detected by Zitrin et al. (2010, see their Fig. 7) from their lensing analysis. Such a spatial segregation between more and less luminous galaxies was found, for instance, in the Coma cluster (Biviano et al. 1996) and, in particular, in the merging cluster Abell 209 (Mercurio et al. 2003a), where bright photometric members are located around the dominant galaxy, while fainter galaxies seem to trace the whole cluster structure in agreement with the X-ray cluster morphology. As in the case of Abell 209 (see also Mercurio et al. 2003b), the segregation observed in A1703 could be interpreted as the result of a merging process caught after the core-core passage, where luminous galaxies trace the remnants of a pre-merging clump hosting the BCG.

Finally, the combined analysis of the velocity and spatial information provides the ultimate evidence of subclustering in A1703. In particular, the classical DS-test detects very significant substructure, with high velocity galaxies mostly located south of the BCG (Fig. 10). The Htree-test makes it possible to identify two main subclusters: G1 and G2 (Fig. 12 and Table 3). G2 hosts the BCG and is populated by high velocity galaxies. G1 exhibits a lower mean velocity and is itself substructured in two subgroups: G11 and G12. G12, in particular, hosts in the bottom of its potential well the galaxy ID 120, placed very close to the 'N' peak (Table 2). Comfortingly, the existence of G11, G12 and G2 is independently confirmed also by the 3D version of

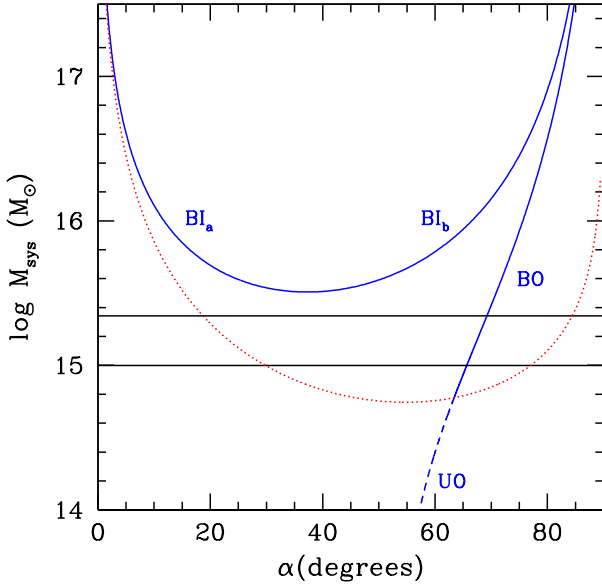


Figure 13. Bound and unbound solutions of the two-body model applied to the subclusters G1 and G2 (thick solid and dashed curves, respectively). The cluster mass is plotted versus the projection angle. Acceptable solutions are the curves intersecting the rectangle defined by the observational values of the cluster mass (bordered by the two horizontal lines). Regions above and below the thin dashed curve are the loci of bound and unbound solutions, respectively, according to the Newtonian criterion of gravitational binding (e.g. Beers et al. 1982).

the adaptive kernel technique (see Table 5). The spatial distribution of G1 and G2 galaxies (see Fig. 12) explains the (marginal) evidence of a velocity gradient (Sect. 5.3) in the direction North-South and is in agreement with the results of the DS-test.

Using the galaxies assigned to G1 and G2 as a first guess when fitting a two groups partition, the 3D-KMM test divides the spectroscopic sample in two subclumps (Table 4). Based on their velocity dispersions we estimate a total mass $M_{200} \sim 1 \times 10^{15} M_{\odot}$ which should be interpreted as a lower limit for the mass of the cluster, being the upper limit $M_{200} \sim 2 \times 10^{15} M_{\odot}$ derived from the measurement of the global velocity dispersion (Sect. 4).

Now, we can adopt the above estimates for the mass of A1703 to study in more detail the merger of the two main subclusters G1 and G2. In particular, we use an analytical two-body model (see, e.g., Lubin et al. 1998 for the details of the method) which is based on the following parameters: M_{sys} , the total mass of the system, D , the projected distance between G1 and G2, and ΔV_{rf} , the relative LOS velocity (in the rest frame). From the biweight estimate of the centres of G1 and G2 we assume $D = 0.46$ Mpc, while their relative velocity is $\Delta V_{\text{rf}} \sim 2000$ km s $^{-1}$. If we also assume that we are seeing the two subclusters at $t = 0.3$ Gyr after the core crossing, which is a typical time suggested by the presence of the suspected radio halo in A1703 (e.g., Brunetti et al. 2009), we can plot a M_{sys} versus α (the projection angle between the plane of the sky and the vector defined by

the centres of G1 and G2) graph for three types of solutions: Bound outgoing (expanding) solutions (BO), bound incoming (collapsing) solutions (BI), and unbound outgoing solutions (UO). The results are reported in Fig. 13. The only acceptable solutions in the estimated range of mass of A1703 are BO solutions with $\alpha \sim 65 - 70$ degrees, i.e. we are seeing a merger quite close to the LOS. This is consistent with the hypothesis that the possible extended radio emission observed in the centre of the cluster is a radio halo. In fact, an eventual central radio relic produced by a shock wave propagating along the LOS is a rare event, being a relic preferentially observed in mergers occurring near the plane of the sky and in the outermost regions of a cluster (e.g. Vazza et al. 2012, Golovich et al. 2019).

In conclusion, the observational scenario suggests that A1703 is a massive cluster undergoing strong dynamical evolution, with two or three subclusters involved in a merging process. This evidence arises despite the cluster appears only slightly elongated in the X-rays, but this is not unusual. Indeed, a non-relaxed state is observed in $\sim 70\%$ of clusters at $z \sim 0.2$ even in the presence in some cases of a regular shape in the X-ray imaging data (Smith et al. 2005). Thus, our results are in agreement with the disturbed dynamics found by Ge et al. (2019) through the study of several X-ray morphological indicators.

In this merging context, the possible presence of a radio halo in the central regions of the cluster would not be surprising, thus we rule out the hypothesis that A1703 could constitute a new intriguing case of a rare relaxed cluster hosting diffuse radio emission.

Finally, our results are in marked contrast with respect to the picture of an unimodal, dynamically relaxed cluster painted by previous studies based on gravitational lensing (see Sect. 1). Since cluster mass profiles inferred from gravitational lensing suffer from complicated lens geometry (see Narayan & Bartelmann 1996 for a general review), if A1703 were a rare relaxed cluster at intermediate redshift it would be of great value to test structure formation in the Λ CDM paradigm through the study of its regular mass distribution. On the contrary, the subclustering we find in A1703 seems to rule out this possibility.

ACKNOWLEDGEMENTS

We thank the anonymous referee for his/her stimulating comments and suggestions.

We are in debt with Federica Govoni for the VLA radio image she kindly provided us. We also thank Luigina Feretti for useful suggestions and discussions.

M.G. acknowledges financial support from the grant MIUR PRIN 2015 ‘‘Cosmology and Fundamental Physics: illuminating the Dark Universe with Euclid’’ and from the University of Trieste through the program ‘‘Finanziamento di Ateneo per progetti di ricerca scientifica - FRA 2018’’.

This publication is based on observations made on the island of La Palma with the Italian Telescopio Nazionale Galileo, which is operated by the Fundaci3n Galileo Galilei-INAf (Istituto Nazionale di Astrofisica) and is located in the Spanish Observatorio de la Roque de los Muchachos of the Instituto de Astrofisica de Canarias.

This research has also benefited from the galaxy cata-

logue of the Sloan Digital Sky Survey (SDSS). The SDSS web site is <http://www.sdss.org/>, where the list of the funding organizations and collaborating institutions can be found.

This research has made use of the NASA/IPAC Extragalactic Database (NED), which is operated by the Jet Propulsion Laboratory, California Institute of Technology, under contract with the National Aeronautics and Space Administration.

This research has also made use of IRAF. This package (ASCL code record 9911.002) is distributed by the National Optical Astronomy Observatory, which is operated by the Association of Universities for Research in Astronomy (AURA) under a cooperative agreement with the National Science Foundation.

REFERENCES

- Abell G. O., 1958, *ApJS*, 3, 211
- Abell G. O., Corwin Jr. H. G., Olowin R. P., 1989, *ApJS*, 70, 1
- Adami C., Giles P., Koulouridis E., et al., 2018, *A&A*, 620, A5
- Allen S. W., Edge A. C., Fabian A. C., et al., 1992, *MNRAS*, 259, 67
- Arnoud M., Pratt G. W., Piffaretti R., et al., 2010, *A&A*, 517, A92
- Ashman K. M., Bird C. M., Zepf S. E., 1994, *AJ*, 108, 2348
- Bayliss M. B., Johnson T., Gladders M. D., Sharon K., Oguri M., 2014, *ApJ*, 783, 41 (B14)
- Beers T. C., Geller M. J., Huchra J. P., 1982, *ApJ*, 257, 23
- Beers T. C., Flynn K., Gebhardt K., 1990, *AJ*, 100, 32
- Bird C. M., Beers, T. C., 1993, *AJ*, 105, 1596
- Bonafede A., Intema H. T., Brüggen M., et al., 2014, *MNRAS*, 444, L44
- Böhringer H., Chon G., Collins C. A., 2014, *A&A*, 570, A31
- Biviano A., Durret F.; Gerbal D., et al., 1996, *A&A*, 311, 95
- Biviano A., Rosati P., Balestra I., et al., 2013, *A&A*, 558, A1
- Boschin W., Girardi M., 2018, *MNRAS*, 480, 1187
- Boschin W., Girardi M., Barrena R., et al., 2004, *A&A*, 416, 839
- Boschin W., Girardi M., Barrena R., 2013, *MNRAS*, 434, 772
- Brunetti G., Cassano R., Dolag K., Setti, G., 2009, *A&A*, 507, 661
- Brunetti G., Jones T. W., 2015, *Magnetic Fields in Diffuse Media*, Astrophysics and Space Science Library, Vol. 407, Springer-Verlag Berlin Heidelberg, p. 557
- Cassano R., Etti S., Giacintucci S., et al., 2010, *ApJ*, 721, L82
- den Hartog R., Katgert P., 1996, *MNRAS*, 279, 349
- Dressler A., 1980, *ApJ*, 236, 351
- Dressler A., Shectman S. A., 1988, *AJ*, 95, 985
- Fadda D., Girardi M., Giuricin G., et al., 1996, *ApJ*, 473, 670
- Feretti L., Giovannini G., Govoni F., Murgia M., 2012, *A&ARv*, 20, 54
- Ge C., Sun M., Rozo E., et al., 2019, *MNRAS*, 484, 1946
- Gebhardt K., Beers T. C., 1991, *ApJ*, 383, 72
- Girardi M., Bardelli S., Barrena R., et al., 2011, *A&A*, 536, A89
- Girardi M., Boschin W., Barrena R., 2010, *A&A*, 517, A65
- Girardi M., Boschin W., De Grandi S., et al., 2019, *A&A*, in press (eprint [arXiv:1908.02277](https://arxiv.org/abs/1908.02277))
- Gitti M., Brunetti G., Cassano R., Etti S., 2018, *A&A*, 617, A11
- Golovich N., Dawson W. A., Wittman D. M., et al., 2019, *ApJ*, 882, 69
- Hennawi J. F., Gladders M. D., Oguri M., et al., 2008, *AJ*, 135, 664
- Koester B. P., McKay T. A., Annis J., et al., 2007, *ApJ*, 660, 239
- Lauer T. R., Postman M., Strauss M. A., Graves G. J., Chisari N. E., 2014, *ApJ*, 797, 82
- Limousin M., Richard J., Kneib J.-P., et al., 2008, *A&A*, 489, 23
- Lubin L. M., Postman M., Oke J. B., 1998, *AJ*, 116, 643
- Mantz A. B., Allen S. W., Morris R. G., et al., 2015, *MNRAS*, 449, 199
- Martel H., Robichaud F., Barai P., 2014, *ApJ*, 786, 79
- Maurogordato S., Sauvageot J. L., Bourdin H., et al., 2011, *A&A*, 525, A79
- Mercurio A., Girardi M., Boschin W., Merluzzi P., Busarello G., 2003a, *A&A*, 397, 431
- Mercurio A., Massarotti M., Merluzzi P., et al., 2003b, *A&A*, 408, 57
- Munari E., Biviano A., Borgani S., Murante G., Fabjan D., 2013, *MNRAS*, 430, 2638
- Narayan R., Bartelmann M., 1996, [arXiv:astro-ph/9606001](https://arxiv.org/abs/astro-ph/9606001), lecture presented at the 13th Jerusalem Winter School in Theoretical Physics: *Formation of Structure in the Universe*, Jerusalem, Israel, 27 Dec 1995 - 5 Jan 1996
- Navarro J. F., Frenk C. S., White S. D. M., 1997, *ApJ*, 490, 493
- Oguri M., Bayliss M. B., Dahle H., et al., 2012, *MNRAS*, 420, 3213
- Oguri M., Hennawi J. F., Gladders M. D., et al., 2009, *ApJ*, 699, 1038
- Owen F., Moirison G., Voges W., 1999, *Diffuse Thermal and Relativistic Plasma in Galaxy Clusters*, MPE Report 271, p. 9
- Piffaretti R., Arnaud M., Pratt G. W., et al., 2011, *A&A*, 534, A109
- Pisani A., 1993, *MNRAS*, 265, 706
- Pisani A., 1996, *MNRAS*, 278, 697
- Planck Collaboration, 2016, *A&A*, 594, A27
- Press W. H., Teukolsky S. A., Vetterling W. T., Flannery B. P., 2007, *Numerical Recipes. The Art of Scientific Computing*, 3rd Edition
- Richard J., Pei L., Limousin M., Jullo E., Kneib J.-P., 2009, *A&A*, 498, 37
- Rizza E., Morrison G. E., Owen F. N., et al., 2003, *AJ*, 126, 119
- Sarazin C. L., 2002, *Merging Processes in Galaxy Clusters*, Astrophysics and Space Science Library, Vol. 272, ed. L. Feretti, I. M. Gioia, & G. Giovannini, pp. 1-38
- Savini F., Bonafede A., Brüggen M., et al., 2018a, *MNRAS*, 478, 2234
- Savini F., Bonafede A., Brüggen M., et al., 2018b, *MNRAS*, 474, 5023
- Serna A., Gerbal D., 1996, *A&A*, 309, 65
- Smith G. P., Kneib J.-P., Smail I., 2005, *MNRAS*, 359, 417
- Sommer M. W., Basu K., Intema H., et al., 2017, *MNRAS*, 466, 966
- Tonry J., Davis M., 1979, *ApJ*, 84, 1511
- van Haarlem M. P., Wise M. W., Gunst A. W., et al., 2013, *A&A*, 556, A2
- van Weeren R. J., de Gasperin F., Akamatsu H., et al., 2019, *Space Sci. Rev.*, 215, 16
- Vazza F., Brüggen M., van Weeren R., et al., 2012, *MNRAS*, 421, 1868
- Venturi T., Rossetti M., Brunetti G., et al., 2017, *A&A*, 603, A125
- Wilber A. G., 2018, PhD Thesis, University of Hamburg, Germany
- Zitrin A., Broadhurst T., Umetsu K., et al., 2010, *MNRAS*, 408, 1916

This paper has been typeset from a $\text{\TeX}/\text{\LaTeX}$ file prepared by the author.

Table 1. Continued.

ID	Source	α, δ (J2000)	r	V (km)	ΔV (s^{-1})
043	B	13 14 21.80,+51 54 28.3	19.60	82689	27
044	B	13 14 22.78,+51 48 55.1	20.03	83906	42
045	B	13 14 23.69,+51 41 55.0	17.35	30183	150
046	B	13 14 26.19,+51 50 20.3	19.25	82893	24
047	B	13 14 27.08,+52 01 14.4	19.79	106429	24
048	B	13 14 32.96,+52 02 12.2	18.98	759027	150
049	B	13 14 33.36,+51 55 04.2	20.39	82611	51
050	B	13 14 34.01,+51 48 11.9	19.85	82707	30
051	B	13 14 34.53,+51 39 47.5	17.56	53363	150
052	B	13 14 35.86,+52 00 11.3	16.88	25995	150
053	B	13 14 38.16,+51 44 43.7	21.72	84428	69
054	B	13 14 38.65,+51 56 10.3	20.17	82281	54
055	B	13 14 38.71,+51 44 07.6	19.56	92369	27
056	L	13 14 41.80,+51 48 57.5	17.12	56244	10
057	B	13 14 42.01,+51 58 42.5	21.28	83045	72
058	L	13 14 42.92,+51 48 16.3	19.95	143644	34
059	B	13 14 44.28,+51 51 03.7	20.34	84679	48
060	B	13 14 45.30,+51 55 15.2	19.64	80920	30
061	B	13 14 45.60,+51 38 52.8	21.01	102172	108
062	T	13 14 45.78,+51 51 05.3	19.96	85369	130
063	B	13 14 46.37,+51 47 52.0	20.15	84134	39
064	B	13 14 47.76,+51 43 43.1	21.59	143346	54
065	B	13 14 48.48,+51 52 46.5	20.90	82956	69
066	B	13 14 48.94,+52 03 24.4	17.77	90741	150
067	B	13 14 49.29,+51 40 48.0	17.63	29904	150
068	B	13 14 49.50,+52 02 23.0	16.78	52874	150
069	B	13 14 50.39,+51 58 46.2	20.58	82485	42
070	B	13 14 50.66,+52 00 58.7	21.08	82488	72
071	T	13 14 51.28,+51 50 07.2	20.29	83357	77
072	L	13 14 51.28,+51 50 11.3	20.41	168269	38
073	T	13 14 51.41,+51 49 41.3	19.28	81636	50
074	B	13 14 52.38,+51 48 14.6	20.60	85846	66
075	B	13 14 52.39,+52 02 20.8	19.17	102700	18
076	B	13 14 52.73,+51 40 31.2	18.23	85060	21
077	B	13 14 52.84,+51 52 41.4	20.34	83657	51
078	T	13 14 53.56,+51 52 19.4	19.79	52842	62
079	T	13 14 54.53,+51 52 21.5	20.72	17931	145
080	T	13 14 54.68,+51 50 55.8	19.58	81561	58
081	L	13 14 54.73,+51 53 16.9	16.85	53548	10
082	T	13 14 55.33,+51 47 53.0	18.79	84662	75
083	L	13 14 55.38,+51 51 46.9	21.25	184791	104
084	B	13 14 55.51,+51 41 03.0	19.65	576687	150

Table 1. Continued.

ID	Source	α, δ (J2000)	r	V (km)	ΔV (s^{-1})
085	B	13 14 55.52,+52 03 45.2	20.44	90810	51
086	B	13 14 55.69,+51 47 19.0	19.91	81514	30
087	T	13 14 55.79,+51 53 02.6	20.32	53080	100
088	B	13 14 55.85,+51 54 28.4	20.72	80851	66
089	T	13 14 56.12,+51 52 57.2	19.38	53618	90
090	B	13 14 56.25,+51 53 09.9	20.99	81151	60
091	T	13 14 56.40,+51 50 52.4	20.87	80925	122
092	L	13 14 56.83,+51 48 53.0	20.79	733766	263
093	T	13 14 56.90,+51 51 00.5	19.84	82293	77
094	T	13 14 57.88,+51 51 41.8	20.46	81642	115
095	B	13 14 58.09,+51 49 16.2	21.19	86520	180
096	T	13 14 58.76,+51 52 14.0	19.39	53872	41
097	B	13 14 58.77,+51 44 22.6	20.42	83594	33
098	T	13 14 58.77,+51 49 50.9	19.30	84116	70
099	T	13 14 59.06,+51 53 13.5	18.20	52547	39
100	T	13 14 59.15,+51 51 38.4	20.15	81889	72
101	T	13 14 59.32,+51 49 46.6	20.01	80833	115
102	T	13 14 59.54,+51 49 57.8	21.11	83505	137
103	B	13 14 59.56,+51 47 52.3	21.06	82725	63
104	B	13 14 59.56,+52 02 44.4	19.70	102763	27
105	T	13 14 59.91,+51 50 10.7	20.59	85323	125
106	T	13 15 00.12,+51 49 05.7	20.00	83368	90
107	T	13 15 00.12,+51 50 30.5	19.89	81193	97
108	T	13 15 00.56,+51 50 03.0	20.84	86270	190
109	T	13 15 02.01,+51 51 06.5	19.72	81248	53
110	T	13 15 02.02,+51 47 47.7	20.40	84399	102
111	B	13 15 02.22,+51 42 37.4	19.99	90645	45
112	B	13 15 02.25,+51 49 51.3	21.27	81154	180
113	T	13 15 02.41,+51 50 19.3	19.09	81157	65
114	T	13 15 02.51,+51 52 19.6	21.10	84816	135
115	T	13 15 02.87,+51 51 48.3	20.50	81548	145
116	T	13 15 02.89,+51 49 43.8	20.41	84247	105
117	T	13 15 03.02,+51 47 02.8	20.07	84860	100e
118	T	13 15 03.03,+51 48 50.5	20.76	86609	117
119	T	13 15 03.14,+51 46 31.5	19.55	84175	55
120	T	13 15 03.19,+51 49 56.7	18.76	81117	67
121	T	13 15 03.32,+51 50 22.2	21.26	82004	117
122	T	13 15 03.33,+51 50 29.7	20.58	81617	56
123	T	13 15 03.39,+51 51 33.6	20.20	80986	97
124	T	13 15 03.57,+51 52 38.1	18.07	82492	36
125	T	13 15 03.90,+51 49 26.8	19.61	84224	57
126	T	13 15 03.92,+51 49 09.9	20.51	80792	120

Table 1. Continued.

ID	Source	α, δ (J2000)	r	V (km)	ΔV (s ⁻¹)
127	T	13 15 03.92, +51 50 44.8	19.92	81334	82
128	B	13 15 04.05, +51 39 51.0	20.35	84110	48
129	T	13 15 04.20, +51 50 04.4	20.26	80779	100
130	B	13 15 04.26, +51 47 50.8	23.42	83942	300
131	T	13 15 04.31, +51 47 22.6	20.55	83922	63
132	T	13 15 04.33, +51 51 33.7	18.48	53157	75e
133	T	13 15 04.35, +51 51 47.1	20.66	82945	92
134	T	13 15 04.50, +51 49 11.1	21.57	84697	145
135	T	13 15 04.84, +51 49 32.0	18.74	81410	65
136	T	13 15 05.00, +51 50 02.7	19.33	83533	72
137	B	13 15 05.04, +51 46 06.3	22.58	87210	150
138	T	13 15 05.04, +51 52 08.2	20.27	81517	105
139	T	13 15 05.10, +51 49 54.0	20.50	81889	102
140	B	13 15 05.18, +52 03 06.9	20.05	81331	30
141	T	13 15 05.24, +51 49 02.6	16.76	84697	75
142	T	13 15 05.28, +51 48 35.3	20.92	83155	80
143	T	13 15 05.29, +51 47 53.1	18.37	79194	32
144	B	13 15 05.32, +51 45 36.5	22.04	82923	150
145	T	13 15 05.50, +51 50 01.7	20.46	81449	72
146	T	13 15 05.75, +51 52 31.7	19.15	83298	54
147	T	13 15 05.92, +51 48 45.1	19.16	82249	65
148	T	13 15 06.02, +51 49 01.4	21.22	79868	97
149	T	13 15 06.17, +51 49 43.0	20.60	83816	75
150	T	13 15 06.24, +51 48 34.9	18.34	82684	117
151	L	13 15 06.36, +51 54 27.9	18.13	82178	12
152	T	13 15 06.52, +51 51 00.5	19.72	26235	100e
153	T	13 15 06.68, +51 48 00.3	20.08	85795	75
154	T	13 15 06.69, +51 47 16.3	19.69	116336	288e
155	T	13 15 06.96, +51 49 25.8	19.69	85901	72
156	T	13 15 07.05, +51 50 49.9	20.46	83602	100
157	T	13 15 07.27, +51 51 20.6	20.07	84067	80
158	T	13 15 07.41, +51 48 22.6	19.05	85381	37
159	T	13 15 07.43, +51 48 37.9	21.34	83013	102
160	B	13 15 07.45, +51 39 35.6	20.00	84730	51
161	T	13 15 07.47, +51 47 36.2	20.81	83184	105
162	T	13 15 07.71, +51 51 03.4	17.80	25921	100e
163	T	13 15 07.83, +51 48 58.0	18.55	84172	62
164	T	13 15 08.08, +51 48 48.6	19.19	84643	82
165	T	13 15 08.08, +51 53 08.0	18.93	85814	49
166	T	13 15 08.11, +51 52 17.0	20.64	81998	97
167	T	13 15 08.19, +51 51 53.9	18.88	82376	42
168	T	13 15 08.21, +51 48 28.9	20.78	87478	106

Table 1. Continued.

ID	Source	α, δ (J2000)	r	V (km)	ΔV (s ⁻¹)
169	B	13 15 08.83, +51 45 45.5	23.01	83372	150
170	B	13 15 08.91, +51 46 22.4	22.31	81094	150
171	T	13 15 08.91, +51 49 06.7	20.99	82229	180
172	T	13 15 09.01, +51 49 55.8	20.43	87915	112
173	T	13 15 09.40, +51 47 21.7	19.78	84361	55
174	T	13 15 09.76, +51 48 21.5	20.74	81446	107e
175	T	13 15 09.97, +51 53 31.5	21.04	184767	60
176	T	13 15 10.01, +51 52 43.6	20.31	124393	165
177	B	13 15 10.05, +51 43 13.3	20.20	83252	45
178	T	13 15 10.11, +51 52 23.2	19.87	93275	107
179	T	13 15 10.15, +51 50 03.2	19.31	82684	117
180	T	13 15 10.18, +51 53 20.0	19.93	52960	100e
181	T	13 15 11.06, +51 49 03.2	17.82	52937	62
182	B	13 15 11.06, +51 46 53.8	21.97	80644	180
183	B	13 15 11.07, +51 45 57.7	21.36	82923	150
184	B	13 15 11.19, +51 48 23.3	20.73	85069	63
185	B	13 15 11.20, +51 44 18.2	20.53	84958	69
186	T	13 15 11.50, +51 46 41.5	19.77	80732	54
187	T	13 15 11.59, +51 49 20.4	19.04	80514	55
188	B	13 15 11.96, +51 45 53.0	20.55	81891	54
189	T	13 15 12.03, +51 47 22.4	19.55	81821	72
190	T	13 15 13.47, +51 50 04.9	19.04	86158	57
191	T	13 15 13.56, +51 49 49.2	19.34	82611	65
192	T	13 15 13.73, +51 49 39.5	20.39	85308	80
193	T	13 15 13.73, +51 49 55.1	20.18	83418	125
194	T	13 15 13.73, +51 51 50.1	20.91	795600	335e
195	T	13 15 13.98, +51 49 10.8	19.75	80841	90
196	T	13 15 14.53, +51 50 03.3	19.63	81590	50
197	T	13 15 14.69, +51 48 17.7	20.18	82642	100
198	T	13 15 14.72, +51 47 20.1	20.43	82698	102
199	T	13 15 14.81, +51 48 30.1	20.36	79793	72
200	T	13 15 15.18, +51 48 04.1	18.90	82526	62
201	T	13 15 16.11, +51 47 46.8	19.66	85026	65
202	T	13 15 16.29, +51 50 23.4	18.86	82002	52
203	B	13 15 17.14, +51 57 05.6	19.90	84035	33
204	B	13 15 17.17, +51 53 57.6	19.44	80425	24
205	B	13 15 17.62, +51 42 00.2	22.14	207031	45
206	T	13 15 17.69, +51 47 25.6	20.32	116791	88
207	B	13 15 18.03, +52 00 55.0	19.80	82938	30
208	B	13 15 18.38, +51 51 41.3	20.21	102454	30
209	T	13 15 18.91, +51 48 43.7	19.48	85388	60
210	T	13 15 19.72, +51 48 08.1	19.66	82082	70

Table 1. Continued.

ID	Source	α, δ (J2000)	r	V (km s ⁻¹)	ΔV
211	B	13 15 19.98,+51 38 42.0	19.81	91425	42
212	B	13 15 20.01,+51 43 40.5	21.30	84344	102
213	B	13 15 21.87,+51 49 03.7	19.06	82020	33
214	B	13 15 23.11,+52 01 25.3	16.85	17784	150
215	B	13 15 24.09,+52 03 59.1	15.75	18020	150
216	T	13 15 24.22,+51 48 18.1	19.67	82459	77
217	B	13 15 24.90,+51 54 58.9	16.80	34545	150
218	B	13 15 25.33,+51 51 06.1	19.12	86208	27
219	T	13 15 26.22,+51 47 55.6	19.80	85366	82
220	B	13 15 26.50,+51 44 53.0	20.06	79502	30
221	B	13 15 26.86,+51 43 26.6	19.66	84155	30
222	B	13 15 28.43,+51 37 52.7	21.40	137335	111
223	B	13 15 29.91,+51 52 57.7	21.08	135929	48
224	B	13 15 29.93,+51 55 44.0	19.58	84053	30
225	B	13 15 31.56,+51 45 34.0	21.26	82521	54
226	B	13 15 33.48,+51 51 16.1	21.35	84607	63
227	B	13 15 33.75,+51 58 54.8	20.39	81948	39
228	B	13 15 43.19,+51 49 50.2	20.19	116071	54
229	B	13 15 44.27,+51 43 33.4	19.18	86715	30
230	B	13 15 45.61,+51 52 01.9	19.19	82593	27
231	B	13 15 45.69,+52 00 28.3	22.39	304781	93
232	B	13 15 46.20,+51 48 23.5	19.14	84032	24
233	B	13 15 46.60,+51 51 25.2	19.36	82686	24
234	B	13 15 50.10,+51 39 16.0	20.85	129262	57
235	B	13 15 51.52,+51 48 47.4	19.80	78333	33
236	B	13 15 52.41,+51 44 41.9	21.29	159684	45
237	B	13 15 52.41,+51 46 41.6	20.63	102907	51
238	B	13 15 53.47,+51 56 58.1	20.38	132484	18
239	B	13 15 55.87,+51 53 13.3	20.10	56832	36
240	B	13 15 59.50,+52 04 14.3	20.44	95229	45
241	B	13 16 00.79,+51 51 07.8	17.12	56613	150
242	B	13 16 01.28,+51 57 00.4	20.38	132517	45
243	B	13 16 04.09,+51 43 47.0	21.54	117054	63
244	B	13 16 08.41,+51 40 25.6	20.93	89371	75
245	B	13 16 13.15,+52 03 27.8	19.93	116766	30
246	B	13 16 13.47,+52 04 54.6	20.95	100044	63
247	B	13 16 13.62,+51 45 08.0	21.08	102475	57
248	B	13 16 13.79,+51 40 25.9	20.12	89287	48
249	B	13 16 15.13,+51 38 48.8	17.37	7414	150
250	B	13 16 17.09,+51 49 02.3	15.92	30006	150
251	B	13 16 17.12,+51 40 34.4	18.07	89866	150
252	B	13 16 17.61,+51 40 32.8	21.62	89671	48

Table 1. Continued.

ID	Source	α, δ (J2000)	r	V (km s ⁻¹)	ΔV
253	B	13 16 19.78,+51 37 59.5	19.42	96146	30
254	B	13 16 21.77,+51 56 56.8	20.48	97516	54
255	B	13 16 22.55,+52 01 04.1	19.61	109346	30
256	B	13 16 24.13,+51 49 42.9	20.99	142701	48
257	B	13 16 24.73,+51 38 19.0	20.60	122696	18
258	B	13 16 25.12,+51 55 06.6	20.19	102853	39
259	B	13 16 26.10,+51 50 24.7	20.34	100245	33
260	B	13 16 26.30,+51 41 28.2	19.80	108648	36
261	B	13 16 28.11,+52 00 23.2	21.30	109409	63
262	B	13 16 29.73,+52 03 47.4	19.42	117642	27
263	B	13 16 33.53,+51 51 53.8	21.20	100386	78
264	B	13 16 34.26,+52 00 07.7	20.16	118847	15
265	B	13 16 35.47,+51 54 28.7	23.11	185215	89
266	B	13 16 37.66,+51 55 11.8	19.93	90768	33
267	B	13 16 41.40,+52 02 21.2	19.89	83510	39
268	B	13 16 41.45,+51 57 22.0	20.07	118202	27
269	B	13 16 43.20,+51 42 56.8	20.89	88894	39
270	B	13 16 43.76,+51 45 54.5	20.52	129894	30
271	B	13 16 45.52,+51 51 29.0	20.95	103099	102
272	B	13 16 46.34,+51 40 53.8	20.81	101519	51
273	B	13 16 46.68,+51 43 34.8	21.09	130098	48
274	B	13 16 47.00,+51 44 11.6	20.59	123820	54
275	B	13 16 48.49,+51 56 30.5	20.73	117273	33
276	B	13 16 49.03,+51 58 13.2	18.85	99969	33
277	B	13 16 49.96,+51 38 07.5	19.17	112059	18
278	B	13 16 51.24,+51 38 27.4	20.59	83435	42